ADVANCED MATERIALS INTERFACES
Open Access
www.advmatinterfaces.de

Check for updates

Multicrystalline, Highly Oriented Thick-Film Silicon from Reduction of Soda-Lime Glass

*Ingrid Schall, Stefan G. Ebbinghaus, Christian Strelow, and Erwin Peiner**

The study describes synthesis and characterization of > 10 µm thick multicrystalline (mc), highly oriented, *p*-doped silicon layers by aluminothermic reduction of low-cost soda-lime glass. X-ray diffraction shows a highly preferred (111)-orientation and excellent crystallinity. Low compressive stress and very good crystallinity are confirmed by the peak position and width of the Raman LO-phonon line, approaching the one of bulk single-crystalline wafer material. Due to strong bonding to the glass substrate layer, spalling is not observed. A conductive aluminum-rich oxide layer is formed underneath the silicon, serving as an electrical back-contact for electronic devices. Using secondary ion mass spectrometry very low concentrations of 10^{14}–10^{15} cm^{-3} of impurities are found originating from the soda-lime glass with an iron content below the detection limit. Furthermore, a plateau-like, very homogenous Al concentration of ≈4×10^{18} cm^{-3} over a thickness of ≈10 µm is found, which corresponds to the solubility of Al in Si at the process temperature. Complete electronic activation within the plateau region is confirmed by carrier concentration measurements using electrochemical capacitance–voltage profiling and Raman spectroscopy. Hole concentrations in the range of few 10^{18} cm^{-3} are beneficial for the *p*-type base material of full-emitter cell mc-silicon photovoltaic devices.

1. Introduction

Crystalline silicon on glass substrates has many possible applications like high-mobility layers for thin-film-transistors,[1] microelectromechanical-systems-based high quality factor gyroscopes,[2] energy harvesters for leadless pacemakers,[3] membrane-free microfluidic thermal flow sensors,[4] or material- and energy-efficient fabrication of absorber layers of thin-film solar cells.[5] All these applications have in common that a silicon layer has to be closely connected to the glass substrate. Sheets of bulk crystalline silicon (sawed, thermic stressed, and ion stacked) or silicon layers epitaxially grown on HF-porosified silicon, which are subsequently ablated, can be bonded on glass using an adhesion promoter.[6] Alternatively, gas-phase deposition of silicon on a glass substrate is feasible, for example by electron-beam evaporation or chemical vapor deposition (CVD). With the latter, the process temperature must be kept low enough not to cause damage to the glass, e.g., using plasma-enhanced (PE) CVD. However, direct deposition on a glass substrate results in amorphous or amorphous-microcrystalline silicon yielding low efficiencies of 6%, 7%, and 9.6%, respectively, when used as absorber material for photovoltaic (PV) power generation.[7]

In the so-called aluminum-induced layer exchange (ALILE) process, a layer of aluminum is evaporated on glass and separated by an oxide layer, followed by the deposition of a silicon layer on top. By annealing this sandwich below the Al–Si eutectic temperature of 577 °C[8] aluminum-induced crystallization (AIC) of the silicon starts, and layer exchange leads to ≈100 nm thick coarse-grained silicon (lateral grain size up to 250 µm) on the glass substrate.[9–11] Unfortunately, the obtained crystalline silicon generally contains a large concentration of Al impurities of 3×10^{19} cm^{-3}, which are only partially activated (≈10 %), while a considerable share of it is incorporated on interstitial sites or at grain boundaries creating deep states.[9] Therefore, AIC silicon cannot directly be applied as absorber material for solar cells, but is used as a seed layer for subsequent deposition of µc silicon, however, with a limited electronic quality due to intra-grain defects.[10] On the other hand, remaining Al at the interface between silicon and glass can be beneficially used as a back contact of a solar cell.[9] As an industrially successful process for the

I. Schall
sameday media GmbH
Am Flatthaus 13, 29640 Schneverdingen, Germany
S. G. Ebbinghaus
Institut für Chemie
Martin-Luther-Universität Halle-Wittenberg
Kurt-Mothes-Str. 2, 06120 Halle, Germany
C. Strelow
Institut für Physikalische Chemie
Universität Hamburg
Grindelallee 117, 20146 Hamburg, Germany
E. Peiner
Institut für Halbleitertechnik/Laboratory for Emerging Nanometrology (LENA)
Technische Universität Braunschweig
Hans-Sommer-Str. 66, 38106 Braunschweig, Germany
E-mail: e.peiner@tu-braunschweig.de

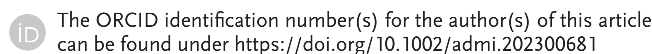
The ORCID identification number(s) for the author(s) of this article can be found under https://doi.org/10.1002/admi.202300681

© 2023 The Authors. Advanced Materials Interfaces published by Wiley-VCH GmbH. This is an open access article under the terms of the Creative Commons Attribution License, which permits use, distribution and reproduction in any medium, provided the original work is properly cited.

DOI: 10.1002/admi.202300681

ADVANCED MATERIALS INTERFACES
Open Access
www.advmatinterfaces.de

production of μc silicon layers on glass, solid-phase crystallization (SPC) was used for solar cell production by CSG Solar AG, Germany until insolvency in 2011.[10] Here, a silicon layer is crystallized by annealing for several hours at a moderate temperature of 600 °C, yielding layer thicknesses and grain sizes of 1–3 μm. With a ≈2 μm thick silicon diode stack by PECVD, treated at ≈600 °C for SPC and subsequently at ≈900 °C for rapid thermal annealing an efficiency of 10.5% was reached. A change of silicon crystallization was considered necessary to overcome the limitations of SPC, e.g., with respect to silicon layer thickness and grain size.

Successful fabrication of thick multicrystalline (mc) silicon wafer material on glass was recently reported based on recrystallizing a deposited silicon layer from its melt.[5,12] Here, at least for good electronic quality, diffusion-barrier-coated, temperature-stable boron-, or alumina-silicate glass substrates are required to achieve mc-silicon layers of a thickness of ≈ 10 μm. The relatively low deposition rate of ≈20 nm min^{-1} of silicon using PECVD can be increased to 1 μm min^{-1} using e-beam evaporation under near ultra-high vacuum conditions. After melting ($T_{m,Si}$ = 1410 °C) the deposited silicon layer crystallizes to grain sizes of ≈100 μm. To limit the thermal load, melting is done only within limited areas by irradiating the glass along consecutive lines using focused halogen lamps, lasers, or an electron beam.[13] The best results by liquid phase crystallization (LPC) are obtained using aluminosilicate glass coated by a triple-stack $SiO_x/SiN_x/SiO$ interlayer (IL).[12] The IL serves as a diffusion barrier to prevent impurities from the glass from entering the silicon while melting. Using a one-side contact system with interdigitated layers of n^+ regions and p^+ emitters, which is needed due to the lack of a back contact, an efficiency of 15.1 % was reached.[5] Small test devices (0.1 cm^2 active area) with a full-emitter cell design, show a maximum efficiency of 15.8%.[12]

IPHT Jena developed an LPC process of Schott Borofloat 33 glass, in which they used a 980 nm diode laser for LPC-film thicknesses > 5 mm for reducing total cost of ownership owing to higher efficiency and lifetime and maintenance-free design in comparison to the standard 808 nm laser process.[14] In their solar cell designs they exploited the transparency of glass for bifacial illumination,[15] or for enabling a textured or nanowire-structured absorber backside surface for efficient light absorption.[16] A low-temperature technology of vanadium oxide/c-Si heterojunctions defined by IR laser processing was proposed for emitter and base contact formation.[17]

Replacing technical glass as a substrate of mc-silicon solar cells with soda-lime glass is the next logical step for further cost reduction. Correspondingly, LPC on soda-lime glass for photovoltaics (PV) was recently reported, however, with a considerably lower PV efficiency of 4.3%.[18] Additionally, occasional spalling of 6 to 12 μm thick silicon layers was observed after a few days with LPC silicon on soda-lime glass substrates. Moreover, Si layers of 12 μm in thickness, which is favored for solar-cell performance, generally peeled off from the triple-stack-coated soda-lime glass substrate after one day at the latest. Stress during solidification of the molten silicon related to the large thermal-expansion mismatch between silicon and soda-lime glass was detected as the root cause of this spalling effect.

A different approach for fabricating silicon on glass is based on the metallothermic reduction of glass. Metallothermic reduction, for example using carbon as the reducing agent, has been widely applied to produce silicon from abundant silicon oxide. Using magnesium or aluminum instead of carbon results in a solid-state process. The chemical reaction of silicon dioxide with aluminum occurs according to

$$3\,SiO_2 + 4\,Al \rightarrow 2\,Al_2O_3 + 3\,Si \quad (1)$$

aluminothermic reduction of the SiO_2 content of a glass surface, e.g., for photovoltaic (PV) application was so far only used for aluminum-induced texturing (AIT) of solar glass for enhancing optical absorption leading to small, non-contiguous μ-crystalline silicon islands. In a detailed study, AIT reduction of planar glass was described, which uses 120 nm sputter-coated aluminum on borosilicate glass at 500–570 °C.[19] Raman measurements showed the typical signature of μc-silicon, i.e., a broad shoulder at the lower wavenumber site of the LO phonon mode with a full width at half maximum of ≈7 cm^{-1} in comparison to monocrystalline bulk silicon (≈3.5 cm^{-1}).[20] A contiguous layer of silicon clusters was formed with a non-uniform thickness in the order of only 100 nm on average. It was assumed that the diffusion of Si atoms through Al_2O_3 nodules is the rate-limiting step in the AIT process.[19] However, the shrinking molecular volumes associated with the aluminothermic reaction (Equation 1), lead to the formation of voids in the produced alumina.[21]

It can be expected that under optimized process conditions the generated alumina does not form a close barrier layer on the glass, which hinders a further transport of aluminum and released silicon for maintaining the reaction, but is rather porous. These pores can be continuously filled by elemental Al from the top layer. The generated silicon, which has a very low solubility in solid aluminum,[8] will be pushed toward the surface, where it can crystallize into an mc layer. This process will not stop until the aluminum is entirely consumed. To prove this concept, we applied the aluminothermic-reduction reaction (Equation 1) and were able to establish a fundamentally novel crystalline-silicon synthesis (CSS) process leading to ≈10 μm mc-silicon layers on standard low-cost soda-lime glass.[22] This CSS process is based on the application of heat (600–650 °C) and pressure (0.05–0.3 MPa) on an aluminum foil. Under these conditions, the Al_2O_3, which is generated during the aluminothermic reaction, does not form a barrier for the continuous transport of Al to the glass surface. The CSS process starts from numerous seeds, which are uniformly distributed across the sample surface. During the process, they coalesce forming a contiguous multicrystalline layer. Therefore, there is no fundamental limitation of the wafer size, but uniformity of the CSS layer requires precise control of the process parameters across the entire glass surface.

CSS was explored and since then continuously optimized on soda-lime glass by sameday media GmbH within three projects funded by the "Deutsche Bundesstiftung Umwelt" (Az 32 945/01, Az 32945/02, Az 32945/03).[23–25]

In the following, we report on > 10 μm thick multicrystalline (mc) silicon layers on low-cost soda-lime glass fabricated using the CSS process and their characteristic properties for device applications, including grain size, crystallinity, strain, impurity distribution, doping level, and conductivity.

© 2023 The Authors. Advanced Materials Interfaces published by Wiley-VCH GmbH

21967350, 2023, 35, Downloaded from https://onlinelibrary.wiley.com/doi/10.1002/admi.202300681 by Fak-Martin Luther Universitats, Wiley Online Library on [11/04/2024]. See the Terms and Conditions (https://onlinelibrary.wiley.com/terms-and-conditions) on Wiley Online Library for rules of use; OA articles are governed by the applicable Creative Commons License

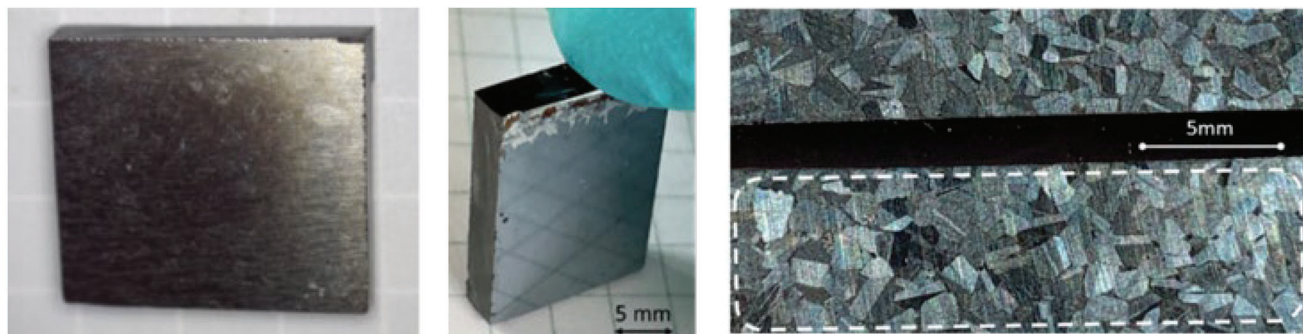

Figure 1. Photographs of silicon layers (13 µm) on soda-lime glass with >2 cm^2 in area prepared via the CSS process after removal of Al residues from the surface by chemical etching (left and middle) and additional polishing to a mirror-like finish with 0.25 µm diamond paste (middle). The right image shows a top-view micrograph of a silicon layer fabricated by area-selective CSS after the removal of Al residues, polishing, and etching in 13.6% NaOH for 2 h. The areas covered with silicon were defined by the pattern of aluminum deposition, i.e., no Al was deposited in the black-stripe area, showing an abrupt transition to the CSS-processed regions.

2. Results and Discussion

To investigate the quality of silicon on soda-lime glass obtained by the CSS process, a detailed characterization was carried out with respect to grain size, crystallinity, strain, impurity distribution, doping level, and conductivity. **Figure 1**, left and middle show photographs of CSS-synthesized crystalline silicon. The remaining unprocessed aluminum in small pits of the silicon or between unconnected silicon crystallites was removed wet chemically using Al80 UN 3265 (see Experimental Section). On the right, a top-view micrograph of a layer is shown after the surface was etched for 2 h by 13.6% NaOH. The surface is completely covered by contiguous grains of silicon extending over ≈1 mm in lateral directions. In this case, two separate areas were processed via CSS by covering these areas with the reducing aluminum layer, while the gap in between was not, i.e., here the unreacted glass surface can be seen. The abrupt transition between the regions, where was the glass converted to silicon, and the unreacted glass impressively visualizes that the CSS process is limited to the area below the aluminum layer, without remarkable penetration of Al in neighboring uncovered regions. This confirms that CSS is not a liquid-phase process, which would cause a more smeared-out silicon growth pattern.

To investigate the crystallinity of the silicon layer, X-ray diffraction measurements were carried out. The result of the $\theta/2\theta$-scan in **Figure 2** measured on an area of ≈1 cm^2 shows a dominant peak at $2\theta \approx 28.5°$ and a second, much smaller one at 56.1°, corresponding to Si (111) and (311), respectively, while the other peaks have 1–2 orders of magnitude lower intensities. The full width at half maximum (FWHM) of the Si (111) peak is 0.05°, which corresponds to the instrumental resolution as determined from measuring single-crystalline silicon under the same conditions. Since in the standard bisecting geometry, only lattice planes parallel to the sample surface contribute to intensities, it follows that for the CSS silicon, the {111} crystal planes are parallel to the surface. This orientation was further verified by rocking-curve measurements (ω-scans), i.e., by tilting the surface normal of the sample while keeping the Bragg angle fixed. In the case of an ideal, perfectly oriented sample, one peak at $\omega = \theta$ is expected. The inset of Figure 2 shows the result for two in-plane orientations of the sample, one arbitrarily chosen and the second after rotating the sample holder by 90° around its surface normal. As can be seen, several peaks appear within an angular range of ≈± 2 °. This indicates a certain mosaicity of the silicon layer, i.e., the presence of several crystallites/crystalline domains in which the {111} lattice planes possess different inclinations with respect to the sample surface. This is in accordance with the micrograph shown in Figure 1. The FWHM of ≈0.3 ° might result from the contributions of additional domains with small-angle tiltings. On the other hand, the FWHM is mainly determined by the divergence of the X-ray beam. For the measurements presented here, a rather large value of 0.6° was chosen in order to illuminate a representative sample area of ≈1 cm^2.

Figure 3 shows on its left art a scanning electron microscope (SEM) image of a cross-section of the sample. The chemical composition was mapped by energy dispersive X-ray spectroscopy (EDX) as shown in the right part of Figure 3 as a false-color representation of the contributions of all relevant elements. The mapped area corresponds to the section of the SEM photograph

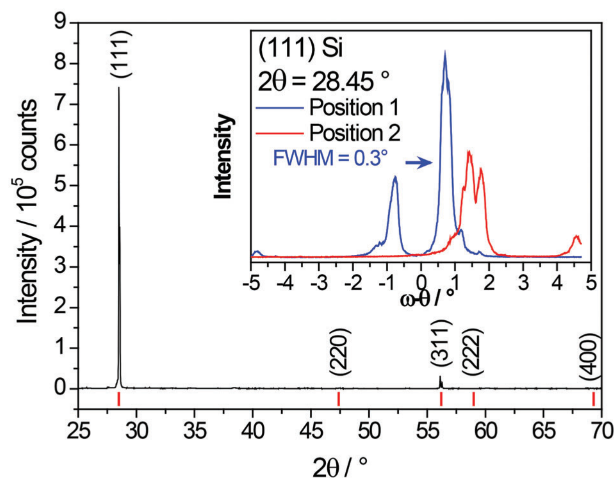

Figure 2. X-ray diffraction pattern ($\theta/2\theta$-scan) of a CSS sample (left). Red tick markers indicate the Bragg angles of silicon. The inset shows two rocking-curve measurements (ω-scan) of the dominant (111) peak for an arbitrary in-plane orientation of the sample and after rotating the sample by 90° about the normal vector to its surface.

© 2023 The Authors. Advanced Materials Interfaces published by Wiley-VCH GmbH

21967350, 2023, 35, Downloaded from https://onlinelibrary.wiley.com/doi/10.1002/admi.202300681 by Fak-Martin Luther Universitats, Wiley Online Library on [11/04/2024]. See the Terms and Conditions (https://onlinelibrary.wiley.com/terms-and-conditions) on Wiley Online Library for rules of use; OA articles are governed by the applicable Creative Commons License

21967350, 2023, 35, Downloaded from https://onlinelibrary.wiley.com/doi/10.1002/admi.202300681 by Fak-Martin Luther Universitats, Wiley Online Library on [11/04/2024]. See the Terms and Conditions (https://onlinelibrary.wiley.com/terms-and-conditions) on Wiley Online Library for rules of use; OA articles are governed by the applicable Creative Commons License

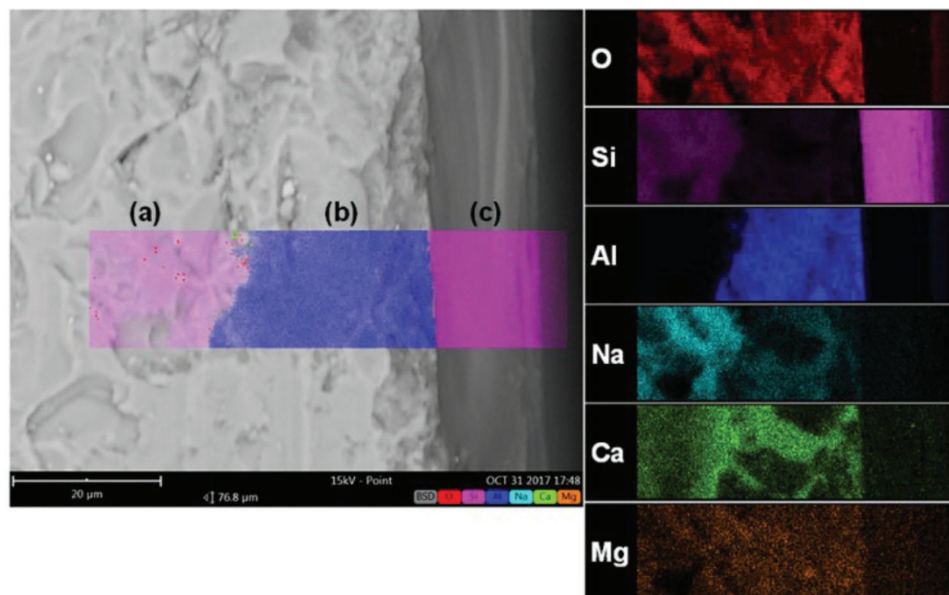

Figure 3. SEM image (left) of a cross-section of the sample shown in Figure 2 with superimposed EDX mapping indicating regions of a) unreacted glass, b) alumina converted from silicon dioxide, and c) synthesized silicon. On the right, the distributions of oxygen (red), silicon (magenta), aluminum (blue), sodium (light blue), calcium (green), and magnesium (brown) in this area are shown.

on the left, where the element distributions of silicon and aluminum are superimposed. From the SEM/EDX image on the left, it is evident, that the silicon layer is the smooth stripe marked as area (c) having a sharp interface to a bright grainy area assigned as the glass substrate. The silicon layer covers the entire surface of the glass, has a uniform thickness of ≈10 µm, and is closely connected to the substrate without any voids. In the superimposed EDX element map the sharp interface coincides with an abrupt transition from silicon to aluminum as the dominating element. Thus, area (b) corresponds to the region, in which the silicon dioxide content of the glass was converted to alumina according to Equation (1), while the unreacted glass is visible in area (a). This interpretation is supported by the oxygen content which is measured across the entire substrate, but not in the silicon layer (upper element map in the right part of Figure 3; Figure S2, Supporting Information).

For further support of this model, we estimate the thickness of the alumina layer (area (b)), which can be expected according to Equation (1). For this, we consider the molecular volumes of silicon dioxide and silicon of 4.3×10^{-23} and 2×10^{-23} cm^3, respectively.[21] The volume ratio of three silicon dioxide formula units reacting to three silicon according to Equation (1) is thus given by $4.3/2 = 2.15$. Since the silicon dioxide content in the used soda-lime glass is 72.6% this ratio increases to $2.25/0.726 = 2.96$. Thus, the thickness of the consumed glass layer should be about three times the thickness of the emerging silicon layer, i.e., ≈30 µm, which is reasonably confirmed by Figure 3 (area (b)) and Figure S2 (Supporting Information). Furthermore, the volume of the consumed silicon dioxide cannot be entirely filled by alumina, since the molecular volumes of SiO_2 and Al_2O_3 (corundum, 4.27×10^{-23} cm^3),[21] are almost equal, but according to Equation (1) three SiO_2 react to only two Al_2O_3. Thus, the volume ratio Al_2O_3/SiO_2 amounts to ≈ 2/3. We therefore assume a porous morphology of the alumina layer with unreacted aluminum left in its pores (Figure S3, Supporting Information). Such an alumina-aluminum composite layer should show electrical conductivity, which was experimentally confirmed as described below.

The alumina-aluminum composite layer (region (b) in Figure 3, left) shows a smooth and sharp interface to the silicon layer, but not to the region of unreacted glass. The content of region (b) is nearly the same as in the unreacted glass, while the silicon signal almost disappeared (Figure S2, Supporting Information). The high content of Al in Figure S2 (Supporting Information) confirms the generation of an aluminum-rich oxidic composite below the silicon layer. EDX maps of sodium, calcium, and magnesium both in the unreacted (a) and converted (b) regions of the substrate (Figure 3, right) reveal similar concentrations (see also Figure S2, Supporting Information). Calcium and sodium show an inhomogeneous distribution, while the Mg content is rather uniform and close to the detection limit of EDX. Only minor changes in the distribution of Mg are visible from the region (a, unreacted glass) to (b, reacted glass) in Figure 3 and Figure S2 (Supporting Information), while the Na signal is considerably weaker in the region (b). Due to its large diffusivity in the unreacted glass, we conclude that Na was removed from region (b) to region (a) of the reacted glass rather than being incorporated into the silicon layer (region (c)). Ca shows a remarkable peak in concentration at the interface between the reacted and the unreacted glass (Figure 3; Figure S2, Supporting Information) indicating segregation. No significant amounts of Al, Na, Ca, or Mg could be detected in the silicon layer, and the apparent small oxygen content is assumed to be an artifact by the residual gas in the SEM chamber.

Crystallization of Si following the aluminothermic reduction of SiO_2 in the CSS process is expected to start at preferential sites,

© 2023 The Authors. Advanced Materials Interfaces published by Wiley-VCH GmbH

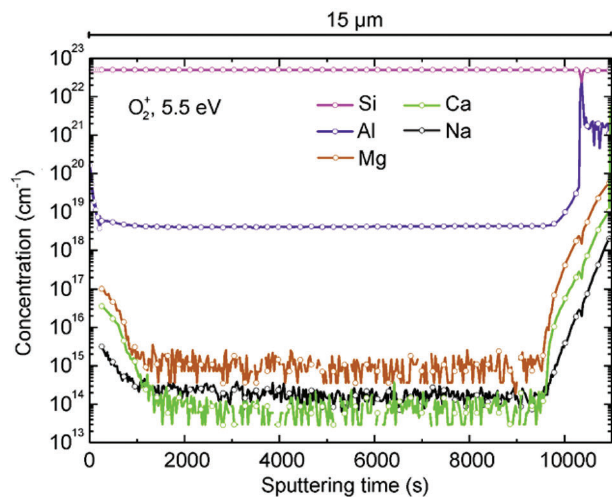

Figure 4. SIMS measurement carried out on the same sample as in the cross-sectional SEM/EDX (see Figure 3). The sputter time is related to depth via the scale bare above the figure.

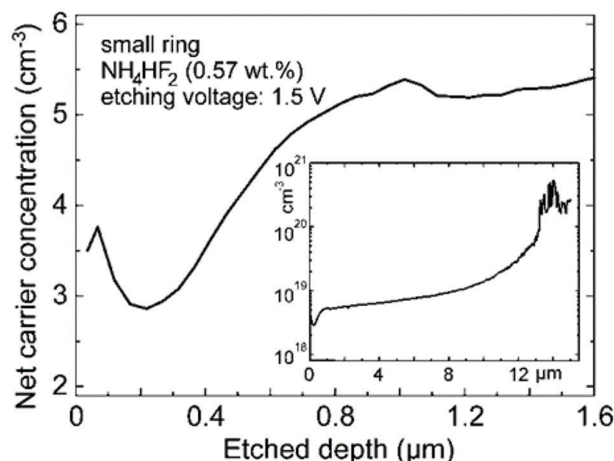

Figure 5. Electrochemical capacitance–voltage (ECV) profile measured on a CSS wafer. The main panel shows the net carrier concentration near the surface with a linear scale while in the inset the data for the entire depth is presented on a logarithmic scale.

e.g., grain boundaries in the Al layer, as known for the AIC/ALILE process.[9–11] Silicon grains will grow in all directions until they reach the top surface of the Al layer. Then, growth will continue laterally until a contiguous layer is formed (Figure 3). Aluminum which has a very low solubility in Si at the process temperature is forced into the opposite direction, toward the glass surface. Here, Al will be quickly consumed by the progressing aluminothermic reaction thereby establishing a concentration gradient for driving diffusion for the supply of further Al. The Al_2O_3 as the second product of the aluminothermic reaction (in addition to silicon, Equation 1) partially fills up the volume of the reacted glass (Figure 3). The remaining space will be filled by unreacted Al. The final structure is therefore mc Si/AlO_x/glass (Figure S1, Supporting Information). CSS proceeds under pressure in normal ambient air[22] and is thus different from a similar process with sputtered Al on quartz performed at 650 or 700 °C under vacuum conditions, resulting in a layer of Si mixed with oxides of Al-related phases.[26]

For trace analysis of the silicon layer secondary ion mass spectrometry (SIMS) was performed. Depth profiles of impurity concentrations in CSS silicon were analyzed by sputtering with 5.5 keV O_2^+ ions on the same sample investigated in the SEM/EDX analyses. **Figure 4** shows the measured concentration profiles of the most relevant elements (Al, Mg, Ca, and Na) over a total sputtering depth of ≈15 µm. Magnesium, calcium, and sodium, whose oxides cannot be reduced by aluminum, exhibit extremely low concentrations in the range of their detection limits. Sulfur, which might be generated by aluminothermic reduction of the sulfate content in the soda-lime glass, is highly volatile and thus not expected to be incorporated in silicon. Moreover, elemental sulfur has a low solubility in solid silicon.[27] Segregation of the measured elements was observed at the top and bottom surfaces of the silicon layer as indicated by elevated concentrations. Most remarkable and highly beneficial for device applications (e.g. solar cells), a constant aluminum concentration of 4×10^{18} cm^{-3} was observed over a large depth range of > 10 µm, again increasing toward the top and bottom borders. The plateau concentration of Al corresponds to the solid solubility of Al in Si at 700 °C[28,29] and is around one order of magnitude lower than the value of 3×10^{19} cm^{-3} reported for aluminum-induced silicon crystallization (AIC).[9] Different from AIC, where a considerable share of Al is incorporated on interstitial sites or at grain boundaries creating deep states for carrier-recombination losses in devices, we find complete activation of the Al dopant atoms in silicon on glass in the CSS process. This was confirmed explicitly by electrochemical capacitance-voltage (ECV) analysis and Raman spectroscopy and is discussed below.

The incorporation of iron may be expected to be caused by the aluminothermic reduction of the Fe_2O_3 content in the soda-lime glass during the CSS process. However, the solubility of iron in silicon at the temperature of the CSS process is six orders of magnitude lower than that of Al,[27] and it is much lower than the total Fe concentration of 3.9×10^{14} cm^{-3} incorporated in cast mc-Si as the dominant PV material.[30] Unfortunately, the SIMS of Al-doped silicon is affected by a mass interference of the used marker ion ($^{54}Fe^+$ isotope) with sputtered Al_2^+ molecules. Thus, calculated concentrations of 1.5×10^{16} cm^{-3} of Fe in the depth range from 1.5 to 6.5 µm represent an upper estimate. A better separation was achieved using an optimized setting with O_2^+ ions of 8 keV. Here, in accordance with the expectation, the Fe concentration was observed to rapidly decrease within ≈1 µm from elevated values at the surface to below the detection limit of SIMS of $\approx 1 \times 10^{15}$ cm^{-3}.

Electrochemical capacitance–voltage (ECV) analysis was done using a CVP21 profiler. **Figure 5** shows the measured net concentration of *p*-type active carriers in a CSS sample yielding $\approx 3 \times 10^{18}$ to $\approx 5 \times 10^{18}$ cm^{-3} in a range starting from the surface to a depth of 1.6 µm.

In this depth range, the ECV measurement nicely corresponds to the Al concentration profiles determined by SIMS except for the steep increase of Al toward the top surface shown in Figure 4. We assign this very large Al concentration $>10^{20}$ cm^{-3} in the first few hundred nm to incomplete ionization, which means that a large amount of Al impurities is not incorporated on

© 2023 The Authors. Advanced Materials Interfaces published by Wiley-VCH GmbH

21967350, 2023, 35, Downloaded from https://onlinelibrary.wiley.com/doi/10.1002/admi.202300681 by Fak-Martin Luther Universitats, Wiley Online Library on [11/04/2024]. See the Terms and Conditions (https://onlinelibrary.wiley.com/terms-and-conditions) on Wiley Online Library for rules of use; OA articles are governed by the applicable Creative Commons License

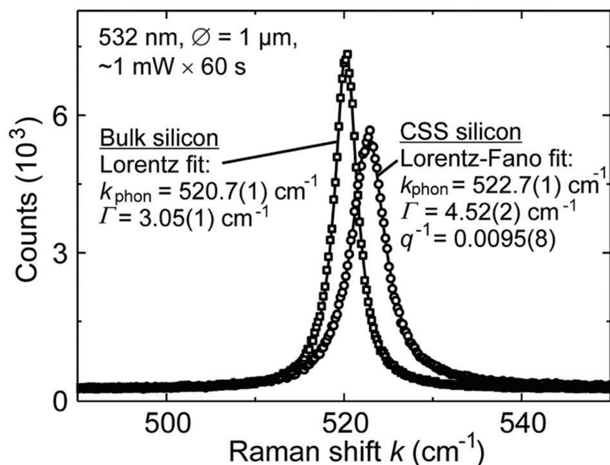

Figure 6. Raman spectrum (λ = 532 nm) of a CSS wafer versus a bulk undoped silicon wafer.

substitutional lattice sites in the silicon. In its bulk regions, however, all Al acceptors are ionized, i.e., occupy substitutional lattice sites. The other impurities (Ca, Na, and Mg) detected by SIMS do not represent dopants in silicon and are thus expected to only negligibly contribute to the net carrier concentration. The steady increase of the ECV profile to hole concentrations $>10^{19}$ cm^{-3} at etch depths beyond ≈5 µm is most probably an artifact of ECV. It can be attributed to an ongoing effective increase of contact area by the developing sidewalls of the etch crater, which is not taken into account in the analysis of the raw data acquired by the ECV profiler and may have caused an apparently higher doping level here.[31] In contrast, the sharp increase of the net charge concentration at ≈13 µm, which is also visible in the SIMS profile of Al, is not an artifact. It indicates that a conductive back-side layer has formed, which can be beneficially used as a bottom contact in devices, e.g., a solar cell.

Further confirmation of the net doping concentrations was obtained from micro-Raman measurements.[32,33] In **Figure 6** a typical Raman spectrum of CSS silicon is depicted revealing essentially the Lorentz-shaped spectral line of optical phonons typical of intrinsic bulk crystalline silicon. Its slight asymmetry is related to doping via coupling of the discrete state of the phonon with the continuum of states by the intraband transitions of the free carriers known as the Fano-resonance effect of Raman scattering.[32]

Asymmetric Raman line shapes can be analyzed using the so-called Lorentz–Fano-fit, where a modified Lorentzian form:[32]

$$I\ (k) = \mathrm{A}\frac{\left(1+\frac{2q^{-1}\left(k-k_{\mathrm{phon}}\right)}{\Gamma}\right)^2}{1+\left[\frac{2\left(k-k_{\mathrm{phon}}\right)}{\Gamma}\right]^2}+y_0 \quad (2)$$

is fitted to the measured curve with the Raman shift k, the peak maximum, and width k_{phon} and Γ, respectively, and the asymmetry factor $1/q$. From the measurement shown in Figure 6, we obtain values of $k = 522.7(1)$, $\Gamma = 4.52(2)$ cm^{-1}, and $1/q = 0.0095(8)$. A linear dependence of $1/q$ on hole concentration in silicon was empirically found.[32] This is used for calculating a value of $p \approx 3 \times 10^{18}$ cm^{-3} of the CSS sample, which is in close agreement with the net carrier-concentration values obtained by ECV, as well as with the impurity concentrations determined by SIMS.

The line width of the Raman peak is characteristic of the crystal quality of the silicon layer. Its value Γ determined by the Lorentz–Fano-fit can be described as the sum of the contributions of Lorentz and Fano distributions, i.e., Γ_{L} and Γ_{F}, respectively:[32]

$$\Gamma = \Gamma_{\mathrm{F}} + \Gamma_{\mathrm{L}} \quad (3)$$

To extract Γ_{L} as the intrinsic width, which is a measure of crystal quality, the Fano broadening Γ_{F} can be estimated according to:[32]

$$\Gamma_{\mathrm{F}} = 2\eta^{5/3}\left(\frac{1}{q}\right)^{2/3};\ \eta = 4.69 \quad (4)$$

Using the determined values of Γ and the inverse asymmetry (Fano) parameter $1/q$, as well as Equations (3) and (4) we obtain $\Gamma_{\mathrm{L}} = 3.35(9)$ cm^{-1}, which is close to the value of 3.05 cm^{-1} measured with undoped bulk single-crystalline silicon. It is lower than the data reported for annealed SPC silicon and LPC silicon on glass of 4.1 and 3.5 cm^{-1}, respectively.[34] This finding nicely demonstrates the very good crystal quality of the CSS material with respect to the other fabrication methods.

Finally, from the shift of the measured Raman peak $k_{\mathrm{phon,CSS}} = 522.7(1)$ cm^{-1} and the value of bulk silicon $k_{\mathrm{phon,bulk}} = 520.7(1)$ cm^{-1} the stress in the CSS material can be calculated:[32,35]

$$\sigma\ (\text{in MPA}) = -250\left[k_{\mathrm{phon,CSS}} - k_{\mathrm{phon,bulk}}\right]\left(\text{in cm}^{-1}\right) \quad (5)$$

The resulting compressive stress value of −500.0(2) MPa is lower than the range of 580 to 850 MPa reported for an LPC-silicon seed layer on Borosilicate glass.[35] This is surprising in view of the much larger thermal expansion coefficient of soda-lime versus Borosilicate glass[18] and the corresponding larger thermal stress to be expected for CSS silicon. Obviously, CSS silicon is less affected by extended lattice defects, such as dislocations, dislocation networks, and grain boundaries, which are considered as the origin of intrinsic stress in LPC silicon.[18] An explanation could be the lower temperature of the CSS process, which is below the melting point of Al. In a further set of measurements an area of 200 × 200 µm^2 of a CSS sample was investigated by scanning Raman spectroscopy using a HeNe laser (λ = 633 nm). A total of 40 × 40 spectra was acquired using a laser spot of 0.8 µm in diameter positioned in a mutual lateral distance of 5 µm. Subsequently, the measured 1600 spectra were evaluated by the Fano fitting analysis described above.

Figure 7 shows the spatial distribution of Raman peak (a), line width (b), and asymmetry factor (c). For the Raman peak an average value of $k_{\mathrm{phon,CSS}} = 522(1)$ cm^{-1} was found, corresponding to an average stress of $\sigma = 325(1)$ MPa. An average intrinsic line width was determined across all spectra using Equations (3) and (4) to $\Gamma_{\mathrm{L}} = 3.4(5)$ cm^{-1}, which again closely approaches the bulk single-crystalline silicon reference of 2.85 cm^{-1} measured with this setup.

The Raman peak asymmetry caused by the Fano effect decreases with the wavelength of the excitation laser.[35] Nevertheless, as described above for the case of 532 nm,[32] linear

© 2023 The Authors. Advanced Materials Interfaces published by Wiley-VCH GmbH

21967350, 2023, 35, Downloaded from https://onlinelibrary.wiley.com/doi/10.1002/admi.202300681 by Fak-Martin Luther Universitats, Wiley Online Library on [11/04/2024]. See the Terms and Conditions (https://onlinelibrary.wiley.com/terms-and-conditions) on Wiley Online Library for rules of use; OA articles are governed by the applicable Creative Commons License

21967350, 2023, 35, Downloaded from https://onlinelibrary.wiley.com/doi/10.1002/admi.202300681 by Fak-Martin Luther Universitats, Wiley Online Library on [11/04/2024]. See the Terms and Conditions (https://onlinelibrary.wiley.com/terms-and-conditions) on Wiley Online Library for rules of use; OA articles are governed by the applicable Creative Commons License

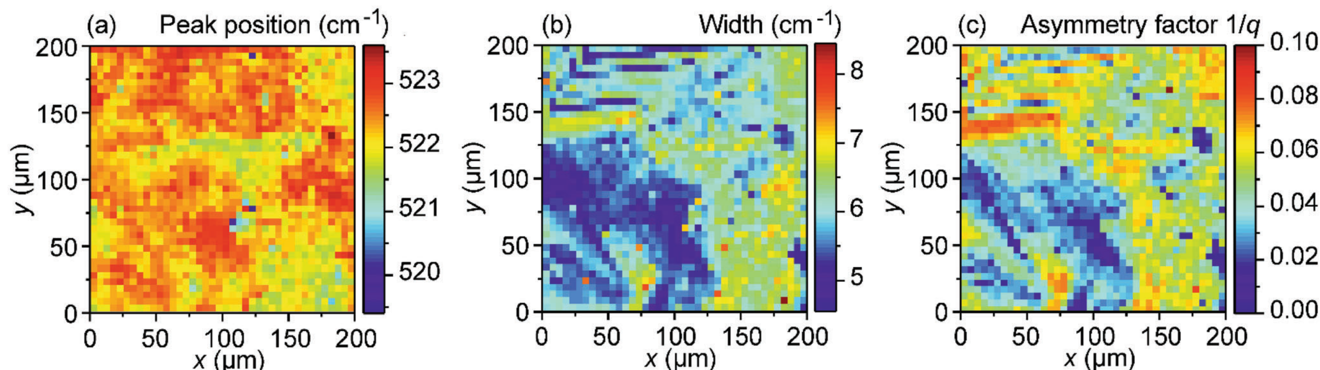

Figure 7. Lateral distribution of a) peak position k_{phon}, b) line width Γ, and c) asymmetry factor $1/q$ of Raman spectra (λ = 633 nm) measured within an area of 200 × 200 µm^2 of a CSS sample.

dependences of $1/q$ versus free carrier concentration were found at 488, 514, and 633 nm.[35] Accordingly, from the average value of the asymmetry factor distribution in Figure 7c of $1/q = 0.045(20)$ at 633 nm a carrier concentration of $p = 4(3) \times 10^{18}$ cm^{-3} is determined, which compares well with both the near-surface net-carrier and dopant concentrations measured by ECV and SIMS, respectively. Excellent fitting results were obtained in all cases using the Lorentz–Fano distribution (Equation 2). Therefore, we rely on this established procedure instead of a recently proposed more sophisticated convoluted Fano–Gaussian function. In that study, doping concentrations extending over a range much larger than relevant for CSS silicon were considered and a linear dependence of $1/q$ versus free carrier concentration was not observed.[33]

To check possible correlations between the parameters obtained from the Raman-line fitting, we depicted them against each other in scatter plots in **Figure 8**a,b. Figure 8a indicates that the half-width tends to decrease with peak position, i.e., the areas of higher compressive stress have better crystallinity. Simultaneously, the half width increases with asymmetry, i.e., low-doped areas have better crystallinity (Figure 8b). This scatter plot of Γ versus $1/q^{2/3}$ shows a sharp lower boundary (indicated as solid line), which extrapolated to $1/q^{2/3} \rightarrow 0$ (intrinsic silicon) yields a value of 2.85 cm^{-1} corresponding to the measured bulk silicon reference value. Analyzing the slope of the solid line using Equation (4) we find $\eta = 3.96$ (for $\lambda = 633$ nm), which is close to $\eta = 4.69$ given in Equation (4) for $\lambda = 532$ nm.[32] The Lorentz component of the line width, which we obtained after subtraction of the Fano component using Equations (3) and (4) with $\eta = 3.96$ is thus independent of doping and a measure of crystalline quality. Excellent crystallinity is revealed by the histogram of $\Gamma_L = \Gamma - \Gamma_F$ in Figure 8c, which has its maximum at 3.44(38) cm^{-1} close to 2.85 cm^{-1} of the bulk single-crystalline silicon reference measured with the same setup.

Under the assumption that all Al impurities are incorporated on substitutional lattice sites, i.e., are fully ionized, the specific resistivity of the p-doped crystalline silicon can be estimated to ≈0.02 Ωcm corresponding to a sheet resistance of R_s ≈20 Ω of a ≈10 µm thick silicon layer. This value is much higher than the one measured by four-point probing of the CSS layer. R_s of 0.9(3) Ω was determined here using fourteen distributed 4P measurements. Obviously, the aluminum oxide scaffold filled with metallic aluminum forms a shunt below the silicon during the measurements. In fact, additional measurements (not discussed here) clearly show that this layer is a good electrical conductor.

In solar cells as a potential application of CSS silicon, concentrations of 3 to 5 × 10^{18} cm^{-3} as base doping (Figure 5) and >10^{12} cm^{-3} for deep-level impurities (Na, Ca, Mg, Figure 4) are known to cause considerable recombination, which may not be acceptable for designs with lateral heterojunction contacts as in the case of LPC silicon on glass. However, different from such cell concepts, the CSS process allows a vertical device architecture with a conventional grid-contacted n-type emitter on top of a bottom-contacted p-type base/absorption layer. The bottom contact is realized by a conductive AlO_x layer resulting from the aluminothermic reaction, which is a composite layer of unreacted Al in an alumina matrix (Figure 3; Figure S3, Supporting Information). Therefore, minority carriers need to travel only over the layer thickness of 10 to 20 µm to the contacts, which is much smaller than the corresponding path length given by the lateral pitch of ≈1 mm of a one-side interdigitated heterojunction contact system in LPC silicon.[12,17] In preliminary photoluminescence (PL) measurements with CSS wafers using a time-correlated single photon counting (TCSPC) method we found lifetimes in the 0.6–3 µs range. Thus, the expected diffusion lengths are close to or exceed the CSS layer thickness several times.[12,17] Furthermore, the net carrier concentration profile in Figure 5 (inset) indicates a pp^+ doping structure of the silicon layer corresponding to an absorber with back-surface field (BSF) beneficial for blocking minority carriers (electrons) from the AlO_x bottom contact.

3. Conclusion

The crystalline silicon synthesis (CSS) process can be applied for fabricating >10 µm thick multicrystalline (mc) silicon layers on low-cost commercial soda-lime glass on the basis of aluminothermic reduction. The layers consist of large grains of ≈1 mm in diameter, which are preferentially oriented within a tilt angle of 1° to 2° with respect to the {111} crystal plane and are slightly compressive-stressed. Crystallinity determined from the width of the Raman LO-phonon line approaches the value of bulk single crystalline wafer material. The CSS silicon layer is atomically bonded to the processed glass substrate via an

© 2023 The Authors. Advanced Materials Interfaces published by Wiley-VCH GmbH

21967350, 2023, 35, Downloaded from https://onlinelibrary.wiley.com/doi/10.1002/admi.202300681 by Fak-Martin Luther Universitats, Wiley Online Library on [11/04/2024]. See the Terms and Conditions (https://onlinelibrary.wiley.com/terms-and-conditions) on Wiley Online Library for rules of use; OA articles are governed by the applicable Creative Commons License

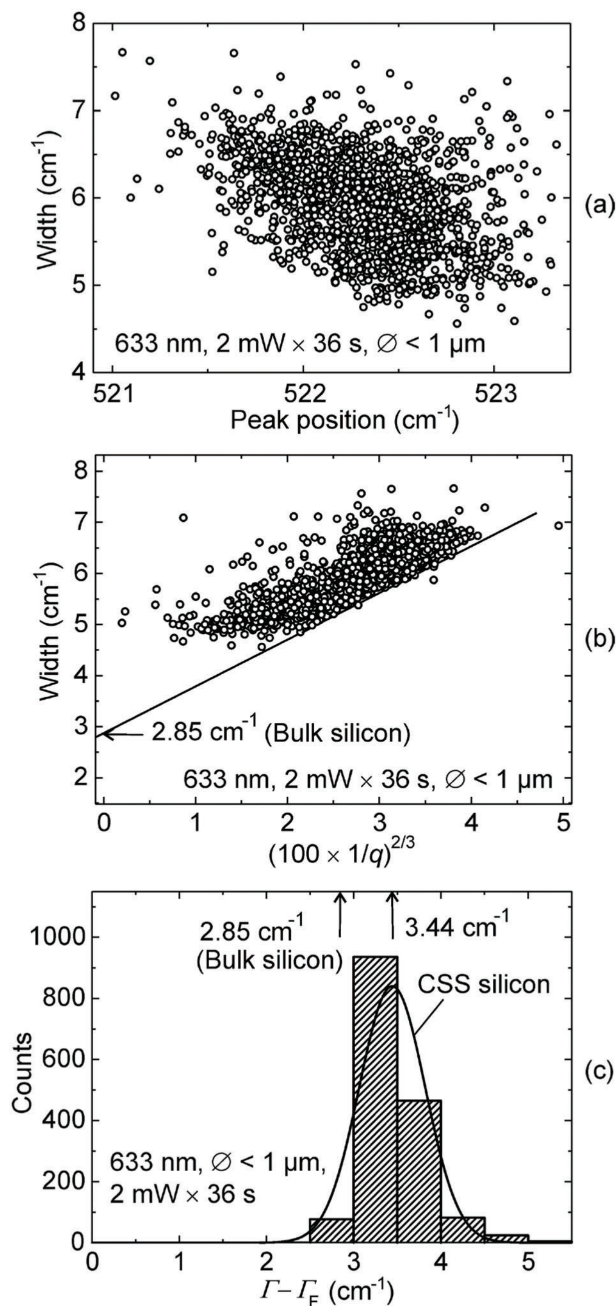

Figure 8. Scatter plots from the results in Figure 7 between selected parameters (a) and (b), and c) the frequency distribution of the Lorentz component of the line width Γ_L obtained after subtracting of the Fano component Γ_F from the measured value Γ. Its average of 3.44(38) cm^{-1} is close to the value of 2.85 cm^{-1} of *p*-doped bulk monocrystalline silicon (at $\lambda = 633$ nm).

alumina interface layer, i.e., strong adhesion is obtained, in contrast to layers on glass fabricated by silicon coating and liquid-phase crystallization. Furthermore, this alumina contains unreacted aluminum, which can be used as an electrical back-contact layer for solar cells. Impurity concentrations determined by secondary ion mass spectrometry (SIMS) show plateau values over the entire ≈10 µm thick silicon layer and increase toward the top and bottom ends. Carrier-concentrations measured using electrochemical capacitance-voltage profiling and Raman spectroscopy within the plateau region show that the aluminum impurities of $\approx 4 \times 10^{18}$ cm^{-3} are completely activated, which is expected according to their solid solubility in silicon at the process temperature of CSS without seriously disrupting the lattice perfection.[36] The other elements present in the soda-lime glass are incorporated in the CSS layer at concentrations of only 10^{14} to 10^{15} cm^{-3} in the plateau region, which are low enough for electronic device applications. Among them, iron has such a low solubility at the CSS process temperature that it cannot be detected by SIMS.

A decisive advantage of CSS over standard liquid-phase crystallization (LPC) is the usage of soda-lime glass, which is about one order of magnitude less expensive than temperature-stable glass. Furthermore, no costly high-vacuum deposition is needed for the CSS process and it is performed under moderate pressure. Finally, for converting the glass into silicon, CSS only requires aluminum in a low amount comparable to the one usually required for back-contact and back surface field (BSF) formation in conventional solar cells. In Table S1 (Supporting Information), the main features of the novel CSS technique are listed in comparison with the respective values of LPC silicon.

The authors have cited additional references within the Supporting Information.[37,38,39]

Supporting Information

Supporting Information is available from the Wiley Online Library or from the author.

Acknowledgements

This work was funded by the Deutsche Bundesstiftung Umwelt (DBU) in three projects (Az.: 32945/01, /02, /03), as well as by the German Federal Ministry for Economic Affairs and Energy (BMWi) and the Lower Saxony Ministry of Science and Culture and Institute for Semiconductor Technology of Technische Universität Braunschweig in a project through the directive of WIPANO (Wissens- und Technologietransfer durch Patente und Normen) under 03THWI009.

Open access funding enabled and organized by Projekt DEAL.

Conflict of Interest

The authors declare no conflict of interest.

Data Availability Statement

The data that support the findings of this study are available from the corresponding author upon reasonable request.

Keywords

aluminothermic reduction, crystal growth, glasses, multicrystalline layers, silicon-on-glass

Received: August 25, 2023
Published online: September 15, 2023

© 2023 The Authors. Advanced Materials Interfaces published by Wiley-VCH GmbH

21967350, 2023, 35, Downloaded from https://onlinelibrary.wiley.com/doi/10.1002/admi.202300681 by Fak-Martin Luther Universitats, Wiley Online Library on [11/04/2024]. See the Terms and Conditions (https://onlinelibrary.wiley.com/terms-and-conditions) on Wiley Online Library for rules of use; OA articles are governed by the applicable Creative Commons License

[1] N. Sasaki, S. Takayama, R. Sasai, Y. Uraoka, *Crystals* **2023**, *13*, 130.
[2] J. Cui, Q. Zhao, *IEEE Transactions on Industrial Electronics*, IEEE, New York, NY **2023**.
[3] F. Ambia, X. Lereoux, A. Harouri, E. Lefeuvre, In 2022 21st Int. Conf. on Micro and Nanotechnology for Power Generation and Energy Conversion Applications (PowerMEMS), IEEE, New York, NY **2022**, pp. 274–277.
[4] V. V. Ryzhkov, V. V. Echeistov, A. V. Zverev, D. A. Baklykov, T. Konstantinova, E. S. Lotkov, P. G. Ryazantcev, R. S. Alibekov, A. K. Kuguk, A. R. Aleksandrov, E. S. Krasko, A. A. Barbasheva, I. A. Ryzhikov, I. A. Rodionov, *Lab Chip* **2023**, *23*, 2789.
[5] S. Garud, C. T. Trinh, D. Abou-Ras, B. Stannowski, R. Schlatmann, B. Rech, D. Amkreutz, *Sol. RRL* **2020**, *4*, 2000058.
[6] P. Montméat, T. Enot, M. D. M. Dutra, M. Pellat, F. Fournel, *Microelectron. Eng.* **2017**, *173*, 13.
[7] G. Parascandolo, G. Bugnon, A. Feltrin, C. Ballif, *Prog. Photovoltaics* **2010**, *18*, 257.
[8] J. L. Murray, A. J. McAlister, *Bull. Alloy Phase Diagrams* **1984**, *5*, 74.
[9] O. Nast, S. Brehme, S. Pritchard, A. G. Aberle, S. R. Wenham, *Sol. Energy Mater. Sol. Cells* **2001**, *65*, 385.
[10] S. Gall, B. Rech, *Sol. Energy Mater. Sol. Cells* **2013**, *119*, 306.
[11] S. M. Kraschewski, *Analytische und In Situ Elektronenmikroskopie zur Metallinduzierten Kristallisation von Silizium*, Friedrich-Alexander-Universitaet Erlangen-Nuernberg, Erlangen, Germany **2018**.
[12] P. Sonntag, N. Preissler, M. Bokalič, M. Trahms, J. Haschke, R. Schlatmann, M. Topič, B. Rech, D. Amkreutz, *Sci. Rep.* **2017**, *7*, 873.
[13] B. Eggleston, S. Varlamov, J. Huang, R. Evans, J. Dore, M. A. Green, *MRS Online Proc. Libr.* **2012**, *1426*, 251.
[14] J. Plentz, T. Schmidt, A. Gawlik, J. Bergmann, G. Andrä, D. Hauschild, V. Lissotschenko, *Phys. Status Solidi A* **2017**, *214*, 1600882.
[15] G. Jia, A. Gawlik, J. Plentz, G. Andrä, *Sol. Energy Mater. Sol. Cells* **2017**, *167*, 102.
[16] M. Vetter, G. Jia, A. Sanei, A. Gawlik, J. Plentz, G. Andrä, *Phys. Status Solidi A* **2017**, *214*, 1600859.
[17] I. Martín, G. López, J. Plentz, C. Jin, P. Ortega, C. Voz, J. Puigdollers, A. Gawlik, G. Jia, G. Andrä, *Phys. Status Solidi A* **2019**, *216*, 19003939.
[18] S. Kühnapfel, S. Severin, N. Kersten, P. Harten, B. Stegemann, S. Gall, *Sol. Energy Mater. Sol. Cells* **2019**, *203*, 110168.
[19] Y. Huang, F. Law, P. I. Widenborg, A. G. Aberle, *J. Cryst. Growth* **2012**, *361*, 121.
[20] A. Lambertz, B. S. Richards, A. B. Sproul, T. Puzzer, M. Gross, In, Proc. 2nd World Conf. on PV Solar Energy Conversion, Vienna, Austria **1998**.
[21] W. T. Tseng, J. P. Stark, *Appl. Phys. Lett.* **1991**, *59*, 680.
[22] G. Palm, E. Peiner, H. Schall, I. Schall, A. Waag, DE102016117182A1 **2016**.
[23] I. Schall, Projekt 32945/01Kristalline Siliziumsynthese auf Quarzsubstrat 'cSi on Quartz' https://www.dbu.de/OPAC/ab/DBU-Abschlussbericht-AZ-32945_01.pdf (accessed 09/23).
[24] I. Schall, Projekt 32945/02, Synthese von multikristallinem Dünnschicht-Silizium für die elektronische Anwendung 'crystalline silicon synthesis (CSS)', https://www.dbu.de/OPAC/ab/DBU-Abschlussbericht-AZ-32945-02.pdf (accessed 09/23).
[25] I. Schall, Projekt 32945/02, Perspektive zur Solarzelle aus der kristallinen Siliziumsynthese 'CSS for solarcell', https://www.dbu.de/OPAC/ab/DBU-Abschlussbericht-AZ-32945_03-Hauptbericht.pdf (accessed 09/23).
[26] M. M. Islam, J. Sawahata, K. Akimoto, T. Sakurai, *Front. Mater.* **2022**, *9*, 977869
[27] K. Tang, E. J. Øvrelid, G. Tranell, M. Tangstad, *Crystal Growth of Si for Solar Cells*, Springer Berlin Heidelberg, Berlin, Germany **2009**, pp. 219–251.
[28] T. Yoshikawa, K. Morita, *J. Electrochem. Soc.* **2009**, *150*, 219.
[29] M. Rauer, C. Schmiga, M. Glatthaar, S. W. Glunz, *IEEE J. Photovoltaics* **2013**, *3*, 206.
[30] P. Zhou, S. Liu, N. Zhou, X. Wei, L. Zhou, *Silicon* **2021**, *14*, 7793.
[31] M. Rauer, M. Rüdiger, C. Schmiga, H. Strutzberg, M. Bähr, M. Glatthaar, S. W. Glunz, *J. Appl. Phys.* **2013**, *114*, 203702.
[32] T. Kunz, M. T. Hessmann, S. Seren, B. Meidel, B. Terheiden, C. J. Brabec, *J. Appl. Phys.* **2013**, *113*, 023514.
[33] S. Palleschi, D. Mastrippolito, P. Benassi, M. Nardone, L. Ottaviano, *Appl. Surf. Sci.* **2021**, *561*, 149691.
[34] C. Becker, D. Amkreutz, T. Sontheimer, V. Preidel, D. Lockau, J. Haschke, L. Jogschies, C. Klimm, J. J. Merkel, P. Plocica, S. Steffens, B. Rech, *Sol. Energy Mater. Sol. Cells* **2013**, *119*, 112.
[35] R. M. B. Agaiby, M. Becker, S. B. Thapa, U. Urmoneit, A. Berger, A. Gawlik, G. Sarau, S. H. Christiansen, *J. Appl. Phys.* **2010**, *107*, 054312.
[36] G. Eranna, *Crystal Growth and Evaluation of Silicon for VLSI and ULSI*, CRC Press, Boca Raton, FL **2014**.
[37] E. Peiner, A. Schlachetzki, *J. Electrochem. Soc.* **1992**, *139*, 552.
[38] E. Peiner, A. Schlachetzki, D. Krüger, *J. Electrochem. Soc.* **1995**, *142*, 576.
[39] C. Schinke, P. C. Peest, J. Schmidt, R. Brendel, K. Bothe, M. R. Vogt, I. Kröger, A. Schirmacher, S. Lim, N. T. Nguyen, D. MacDonald, *AIP Adv.* **2015**, *5*, 067168.

© 2023 The Authors. Advanced Materials Interfaces published by Wiley-VCH GmbH